



Application and validity of the effective medium approximation to the optical properties of nano-textured silicon coated with a dielectric layer

TSUN HANG FUNG,^{1,*} TOM VEEKEN,² DAVID PAYNE,^{1,3} BINESH VEETTIL,^{1,3} ALBERT POLMAN,² AND MALCOLM ABBOTT¹

¹School of Photovoltaic and Renewable Energy Engineering, UNSW Sydney, NSW 2052, Australia

²Center for Nanophotonics, AMOLF, Amsterdam, The Netherlands

³School of Engineering, Macquarie University, Sydney, NSW 2109, Australia

*tsun.fung@unsw.edu.au

Abstract: The emergence of nanotextures in photovoltaics has resulted in challenges associated with optical modelling. Whilst rigorous methods exist to accurately solve these textures, the computational effort required limits the scope of modeling applications. The effective medium approximation (EMA) is a potential alternative to provide rapid modeling results which can be easily integrated with ray tracing of large complex structures. However, the validity of this technique is strongly dependent on the size of features relative to the wavelength of interest, making the application of EMA ambiguous for many situations. This paper aims to address this issue by comparing the simulated results between EMA and finite element methods for three randomly distributed silicon textures with and without a dielectric layer. Criteria for which the EMA approach is valid are proposed and generalized using ratios between root-mean-square roughness, correlation length and incident wavelength, making these limits broadly applicable, beyond that of just the nanotexture under specific solar spectrum regimes. The results in this work apply to random, isotropic textures under normally incident light. Based on the proposed criteria, the validity of different optical simulation techniques for a set of industrial photovoltaic textures is discussed. This analysis reveals a region within which neither geometric optics nor EMA are adequate for calculating the reflectivity of a textured surface, and hence FDTD or other new approaches are required.

© 2019 Optical Society of America under the terms of the [OSA Open Access Publishing Agreement](#)

1. Introduction

Photovoltaics provides a significant market share of the world's electricity generation with a cumulative installed power over 500 GW by the end of 2018 [1]. Modelling is widely used in the industry to develop new technology, to optimise products and to predict the energy yield from large systems [2,3]. Solving the wavelength dependence of light coupling and trapping in the cell, module and system (e.g. via ray tracing) is one option being developed to provide more accurate results [4–6]. This approach relies on rapid techniques to solve the reflection, transmission and absorption at all the many optical interfaces between materials. This paper focuses on a specific aspect of this problem which is the interaction between the surface texture of a solar cell and the relevant wavelengths of light, particularly for the case where the texture contains nano-scaled features (e.g. black silicon). It examines the use of the effective medium approximation to simulate the solar cell front surface and compares the results to those determined via more rigorous techniques such as numerical Finite Difference Time Domain (FDTD) simulations which converge to exact solutions. The geometry studied is particularly relevant within the solar community to the optimisation of black silicon textures and the detailed calculation of module operating temperatures [7,8]. Its relevance extends to the more general development

of nanotextures (particularly where they are coated with dielectric layers) for a broad range of applications [9–11].

Finite Difference Time Domain (FDTD) techniques are well known to simulate light propagation at sub-wavelength scales and provide exact solutions to Maxwell's equations. If done properly, this simulation method provides the most accurate optical simulation results. Several studies have applied FDTD to understand and model the optical behaviour of nanotextured silicon [12–15]. In particular, Kroll *et al.* expanded such simulations with incoherent propagation within the silicon substrate in an attempt to simulate the absorption of the whole silicon wafer [14]. Due to the large simulation volume such simulations are computationally demanding and generally hard to apply to large areas. Another solution is to apply rigorous coupled wave analysis (RCWA) which is a semi-analytical method and ideal for studying scattering of periodic structures like grating devices [16]. The applicability of RCWA on studying nanotextured silicon has also been investigated and found to provide accurate solutions [15]. However, since typical nanotextured silicon is randomly distributed, a relatively large unit cell is required to capture all features in the simulation geometry. As a result, the wavelength range in that study was limited to a 100 nm bandwidth near the Si band edge in order to save computation power. This issue was further investigated by Tucher *et al.* where a field stitching method was applied to replace a large unit cell with several sub-cells and a field-averaging algorithm was used to smoothen the discontinuity in the overlapping regions [17]. However, there is still a restriction on the minimum size of the sub-cell which limits the computational advantage of that method.

Another challenge of rigorous optical simulation of industrial solar cells is the propagation of light through the bulk of the wafers ($\sim 180 \mu\text{m}$ thick) and the interaction with the rear side of the wafers. One option to address the speed issue of both FDTD and RCWA is to derive a scattering matrix that describes the scattering efficiency for a discrete set of input and output angles. This can then be combined with ray tracing to solve for light absorption in the thick wafer, a method also referred to as OPTOS [18] or AMF [19]. There are some situations where that approach has worked well [20,21]. However, deriving the scattering matrix can still be computationally demanding and the solution space is limited to 1 dimension.

An alternative approach is to simply model the textured surface layer with optical material properties determined using an effective medium approximation (EMA) [22]. This analytical approach has previously been applied to simulate the reflection of silicon nanowires for photovoltaic applications, where a single effective medium layer was used [23]. However, typical nanotextures for silicon solar cell applications have a gradual change in volume fraction which leads to an effective refractive index gradient rather than a single thin film [24]. This property was captured by a study where good agreement between EMA and RCWA was achieved in the infra-red region ($2 \mu\text{m} - 10 \mu\text{m}$) [21]. This has implications for modelling devices that operate in those regions, such as photodetectors. It is also relevant to more detailed solving of the operating temperature of silicon solar cells that parasitically absorb longer wavelengths of light leading to substrate heating and a reduction in cell efficiency. However, given the fact that the feature sizes of textured Si wafers are at or below the wavelength of the spectral band where light is absorbed in the solar cell, the validity of EMA for solar cell applications still requires further investigation.

Tang *et al.* investigated the reflectivity of one-dimensional surface profiles characterized by their root-mean squared roughness (σ) and correlation length (τ) [25]. The reflectivity spectra were calculated by an exact approach based on the extinction theorem in the electromagnetic theory and compared to the geometric optics approximation where ray-tracing was used. Criteria for determining when geometric optics is a good approximation of the electromagnetic theory were proposed and generalized using ratios between σ , τ_L and λ , making it applicable to textures of different size. In this work we perform a similar analysis to investigate the validity of the effective medium approximation regarding its ability to predict the reflection and absorption of light in textured silicon.

In this work, we aim to: (1) outline a systematic approach for converting surface topography into appropriate effective medium layers (2) investigate the criteria for which EMA is a good approximation of exact electromagnetic theory models of the optical properties of nanotextured silicon, (3) apply EMA to model nanotextured silicon, both bare and with a conformal dielectric layer. The work does this for normally incident light and assesses agreement in terms of front surface reflection and absorption in the nanotexture.

2. Methods

Randomly distributed nano-scaled surfaces were computationally generated, and the optical properties were modelled by EMA and FDTD in the wavelength range of 300 nm to 2500 nm. We have assumed semi-infinite substrates to enable a direct comparison of FDTD and EMA models, focusing on the effect of front textures. Adding the effect of back-reflection would provide the same effect for both models and will not affect the conclusions. Furthermore, Sunlight has a coherence length of several 10s of microns, which is much larger than the considered feature sizes. As a result, only coherent treatment is considered in this work. In addition to the total front surface reflectance, two-dimensional cross-cuts of the electric field intensity distribution were recorded from the FDTD calculations, which assist in the discussion of the limitations of EMA for photovoltaic applications. We chose to use computer-generated surfaces because it is in practice very difficult to accurately measure the surface topography of nanotextures, and we would prefer to avoid the complication of additional experimental noise in determining the validity of the effective medium technique. It also avoids the question of how to fabricate a texture with the desired surface height distribution. The final section of this work includes some AFM measurements of typical solar cell textures. These measurements were made using Bruker Dimension ICON SPM. A diamond-like carbon coated silicon probe (TESPD) with a nominal tip radius of 18 nm was used for industrially acquired random pyramid texture and metal-assisted chemical texture. A minimum 5:1 high aspect ratio probe (TESPA-HAR) with a nominal tip radius of 10 nm was explicitly used for academic produced reactive-ion etched (RIE) textures. The preparation of the RIE textures were described in [26,27].

2.1. Generation of random surfaces

Each surface morphology was created assuming a Gaussian distribution of heights specified by a set of targeted root-mean-square roughness (σ) and auto-correlation length (τ) using common definitions [28]. Both surface height distribution and correlation length of these surfaces were described by a Gaussian distribution. An open source random surface generator was obtained and further modified to create the sets of homogeneous surfaces used in this study [29]. The shape of underlying features in each surface was created by producing numbers of sinusoidal waves with different frequency. The actual values of σ and τ were confirmed by importing each surface into *Gwyddion*, a common open-source program for AFM data analysis, and using the software's surface statistics function to ensure that actual parameters are within 5 nm of the targeted values [30]. Figure 1 shows the line profile of three textures studied in this work. Texture 1 has an effective slope index (σ/τ_L) of 3, which represents a more needle-like surface. Textures 2 and 3 have smaller effective slope index, representing more planar surfaces.

Figure 2 shows the diagram of “effective slope index versus wavelength-normalized roughness” proposed by Tang *et al.* The blue and green areas in the diagram represent geometries where electromagnetic theory can be approximated by geometric optics, with the green area being valid if only the specular component of total reflectance is concerned. The Textures 1, 2 and 3 examined in this work at different wavelengths were created with pairs of σ and τ_L that fall into the “electromagnetic region” for wavelengths in the range 300-1200 nm for which geometric optics will not work, as we previously confirmed for other experimentally produced photovoltaic nanotextures [31]. The orange region is the effective medium region proposed in this work (based

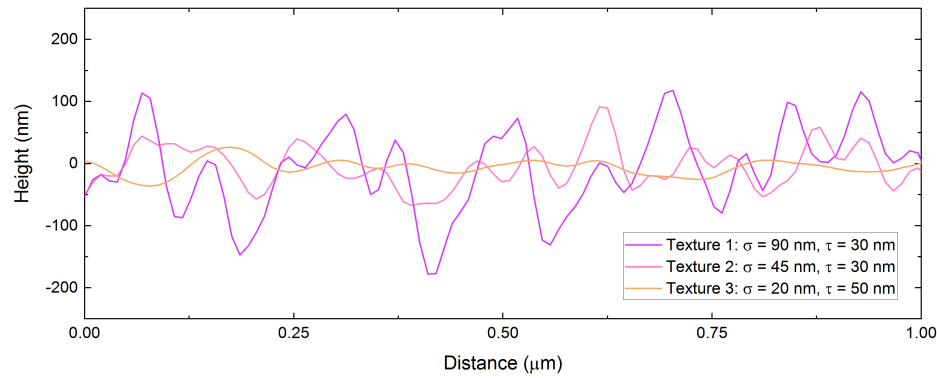


Fig. 1. Line profiles for the artificially created Textures 1, 2 and 3.

on the results presented in Section 3.2), within which the total reflectance of textured silicon can be approximated by EMA. In this study, the proposed criterion for EMA being valid is that the absolute difference in total reflectance between EMA and FDTD must be less than 2%. In this case, the mismatch between two simulation approaches results in less than 1 mA/cm^2 difference in photon current between 300 nm – 1200 nm under the AM1.5G spectrum. It should be reiterated that the criterion proposed in this work only examines the total reflectance for normally incident light and its angular dependency is not within the scope of this study.

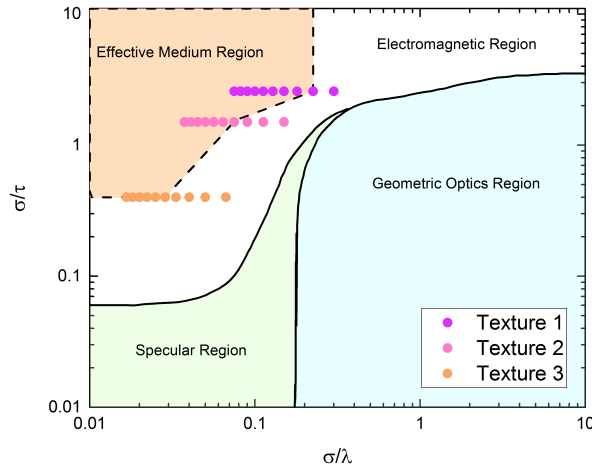


Fig. 2. Diagram of effective slope index versus wavelength-normalized roughness after Tang et al. [25] with regions of specular reflection (green), geometric optics (blue), and the electrodynamic region. The effective medium region (orange) is proposed in this work. Each dot indicates one of the textures at a 100 nm wavelength interval between 300 and 1200 nm (right to left) for normally incident light.

2.2. Summary of EMA simulation

The created nanotextures were modelled as a stack of 20 thin films with each layer designated an effective index corresponding to the materials gradient from air to silicon (Fig. 3). This number of layers was chosen such that the reflectance does not change with further increase in number of

layers and such that no interference fringes were observed. The effective medium method used to calculate the effective permittivity of each layer is described in Section 2.3 and the extraction of volume fraction of each element in each layer is described in Section 2.4. The calculated effective index of each layer was used in a transfer matrix model to calculate the effective specular reflectivity. Both EMA and FDTD models shared the same refractive index ($n + ik$), for silicon [32].

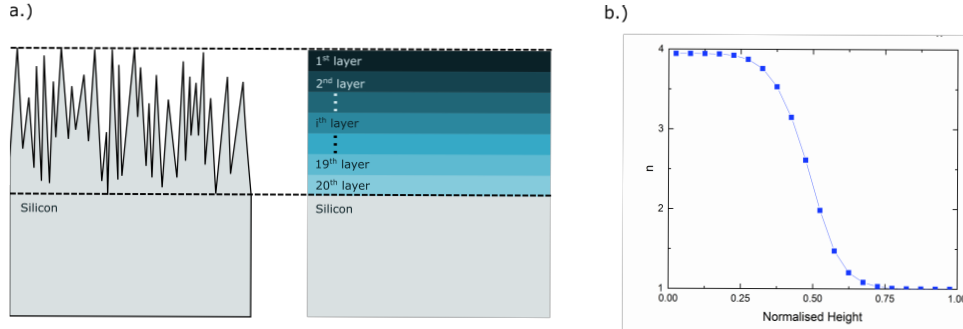


Fig. 3. (a) Schematic diagram on the effective medium approach, where the nano-texture on the surface is modelled as an effective medium which consists of a stack of 20 thin films. (b) The real component of refractive index ($\lambda=600\text{ nm}$) through the height of the effective medium, calculated by the Bruggeman effective medium model for a silicon surface with Gaussian height distribution in air.

2.3. Effective medium theory

Effective medium theory represents the optical properties of a complex composite by an effective homogenous medium. It has been successfully used to represent the effective optical properties of nanoparticles, porous silicon, mesocrystal and gratings [33–36]. Recently, it has also been applied to nanotextured silicon [21,23].

Several different models have been developed with regards to calculating the optical properties of the mixed effective medium. The Maxwell-Garnett model is one of the most studied mixing formulae, originally derived for spherical inclusions in a host medium [37]. It works best for dilute composites due to its asymmetry property between the permittivity of host and inclusion [38]. Due to the same property, it cannot be generalized for modelling composite of three materials. As such, it is not applicable for modelling textured silicon in this work. We use the well-known Bruggeman mixing model which, for a mixture of two dielectric media states

$$f_{Si} \left(\frac{\varepsilon_{Si} - \varepsilon_{BG}}{\varepsilon_{Si} + 2\varepsilon_{BG}} \right) + (1 - f_{Si}) \left(\frac{1 - \varepsilon_{BG}}{1 + 2\varepsilon_{BG}} \right) = 0, \quad (1)$$

with f_{Si} the volume fractions of Si and ε_{Si} and ε_{BG} the dielectric constants of Si and the modelled effective constant, respectively. This equation can be factorized into a second-order polynomial [38,39]

$$0 = A\varepsilon_{BG}^2 + B\varepsilon_{BG} + C, \quad (2)$$

where

$$A = -2; B = f_{Si}(2\varepsilon_{Si} - 1) + (1 - f_{Si})(2\varepsilon_{air} - \varepsilon_{Si}); C = \varepsilon_{Si}.$$

To model the effective permittivity of nanotextured silicon coated with a dielectric layer, the BG equation becomes.

$$f_{Si} \left(\frac{\varepsilon_{Si} - \varepsilon_{BG}}{\varepsilon_{Si} + 2\varepsilon_{BG}} \right) + f_d \left(\frac{\varepsilon_d - \varepsilon_{BG}}{\varepsilon_d + 2\varepsilon_{BG}} \right) + (1 - f_{Si} - f_d) \left(\frac{1 - \varepsilon_{BG}}{1 + 2\varepsilon_{BG}} \right) = 0, \quad (3)$$

With f_d and ε_d the volume fractions of dielectric coating and dielectric constant of the coating, respectively. It can be factorized into a third-order polynomial

$$0 = D\varepsilon_{BG}^3 + E\varepsilon_{BG}^2 + F\varepsilon_{BG} + G, \quad (4)$$

where

$$\begin{aligned} D &= -4, \\ E &= (6f_{Si} - 2)\varepsilon_{Si} + (6f_d - 2)\varepsilon_d + (4 - 6f_{Si} - 6f_d), \\ F &= (3f_{Si} + 3f_d - 1)\varepsilon_{Si}\varepsilon_d + (2 - 3f_d)\varepsilon_{Si} + (2 - 3f_{Si})\varepsilon_d, \\ G &= \varepsilon_{Si}\varepsilon_d. \end{aligned}$$

For both polynomials, only one root resulted in positive values for n and k. The other(s) resulted in negative numbers, which are discarded [38,39].

2.4. Extraction of volume fraction for individual element

Figure 4 shows the cumulative height distribution ($P(z)$) of Texture 1 extracted by *Gywddion*. It is equivalent to the bearing area curve which gives the ratio of air to materials at any height (z), irrespective to the shape of the texture, number of materials, and randomness of the spatial distribution [28]. For a coated silicon surface, a 100 nm thick conformal layer was added on top of the generated texture. This is approximately equivalent to a directed deposition process. The addition of this layer causes the $P(z)$ to be shifted by 100 nm towards the positive z direction, such that

$$P'(z) = P(z + 100), \quad (5)$$

where $P'(z)$ is the cumulative height distribution of the passivated silicon surface. For the texture coated with dielectric, the volume fraction of silicon (v_{Si}) at height z is

$$v_{Si} = 1 - P(z), \quad (6)$$

the volume fraction of air (v_{air}) at height z is

$$v_{air} = P'(z), \quad (7)$$

and the volume fraction of dielectric layer (v_d) at height z is

$$v_d = 1 - P'(z) - P(z). \quad (8)$$

2.5. Details of numerical FDTD calculation

The reflection and absorption spectra were calculated using finite-difference time-domain (FDTD) calculations performed in Lumerical FDTD Solutions [40]. The surface textures of $5 \times 5 \mu\text{m}$ were imported and placed in a simulation box of $5 \times 5 \times 1.4 \mu\text{m}$. For the calculations of textures with a dielectric coating, the same surface was copied and displaced in the lateral direction to mimic conformal coating of the Si texture. Periodic boundary conditions were employed in the surface texture plane, while perfectly matching layers (PMLs) were used in the lateral directions. A broadband plane wave source was employed under normal incidence propagating in the negative z-direction. To calculate the reflection from the texture, a power monitor was placed above the source; to calculate the absorption in the surface texture, two power monitors were placed at the beginning and end of the texture, respectively. To obtain the two-dimensional cross-cut of the electric field intensity distribution, a field monitor was placed in the x-z plane that recorded the electric field intensity of the propagating plane wave with 100 nm wavelength intervals. Mesh

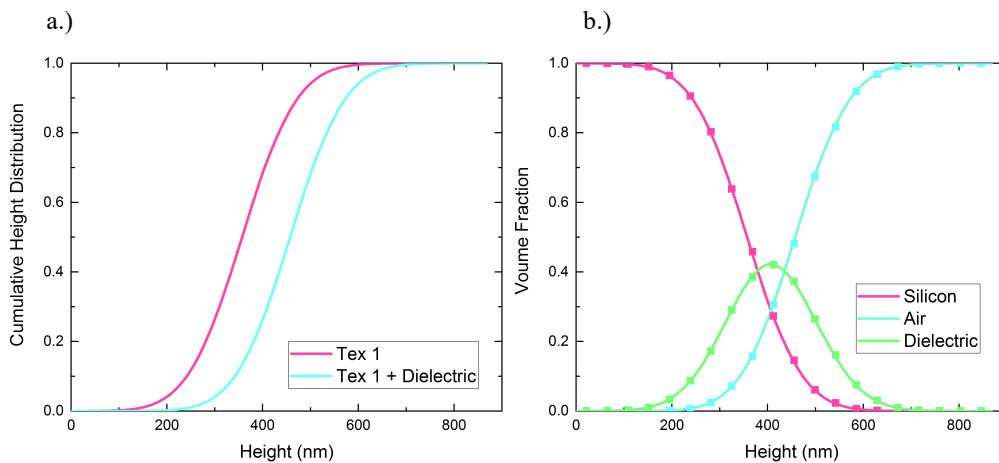


Fig. 4. Cumulative height distribution of Texture 1 with and without dielectric (a) and volume fraction of each component in Texture 1 coated with dielectric (b).

resolution convergence was found for a 3 nm mesh in all three dimensions, with conformal mesh refinement. The calculations were performed on a computer cluster, using 512 CPU's in parallel with 4GB RAM per CPU. To remain within the memory capacity, the calculations were carried out over two wavelength regimes: 300-1400 nm and 1400-2500 nm. To ensure identical optical properties for the materials in both wavelength regimes, the optical constants (n and k) were fitted with analytical functions over the full range (300-2500 nm) for both simulations. Literature values of the optical constants of Si were used [32]. The n and k values of the dielectric were set to equal 2 and 0, respectively, for all wavelengths.

3. Results

3.1. Effective medium approximation for bare silicon

Figure 5 shows the reflectance and absorptance spectra of the bare silicon textures from the EMA model compared to the FDTD calculations. Excellent agreement is found for the simulated reflectance between the EMA model and FDTD calculations above 370 nm (Texture 1), 590 nm (Texture 2), and 700 nm (Texture 3), where the absolute difference in reflectance between EMA model and FDTD calculations is less than 2% absolute (Fig. 6(a)). However, the simulated reflectance by EMA shows significant disagreement with FDTD in the short wavelength region for all textures, indicating that the EMA model is not valid within this region. As λ reduces, the σ/λ increases and the value of σ/λ beyond which deviation started to occur ($\sigma/\lambda_{\text{critical}}$) seems to depend on the value of effective slope index (σ/τ). In other words, the validity of EMA on textures with higher effective slope index extends to shorter wavelengths. In the short wavelength region, the EMA model consistently underestimates the reflectivity for all textures (Fig. 6(a)). The discrepancy between these models appears to be more significant when the effective slope index of the textures is smaller. The absolute difference in reflection at 300 nm between EMA and FDTD is 2% for Texture 1 and is as large as 20% for Texture 3. For a given volume fraction (e.g. $f_{\text{Air}} = f_{\text{Si}} = 0.5$), the in-plane dimensions of individual elements in middle and deep layers is larger for planar texture (smaller effective slope index) as compared to that of more needle like textures (larger effective slope index). As the individual elements get larger and closer to the incident wavelength, EMA starts to perform poorly.

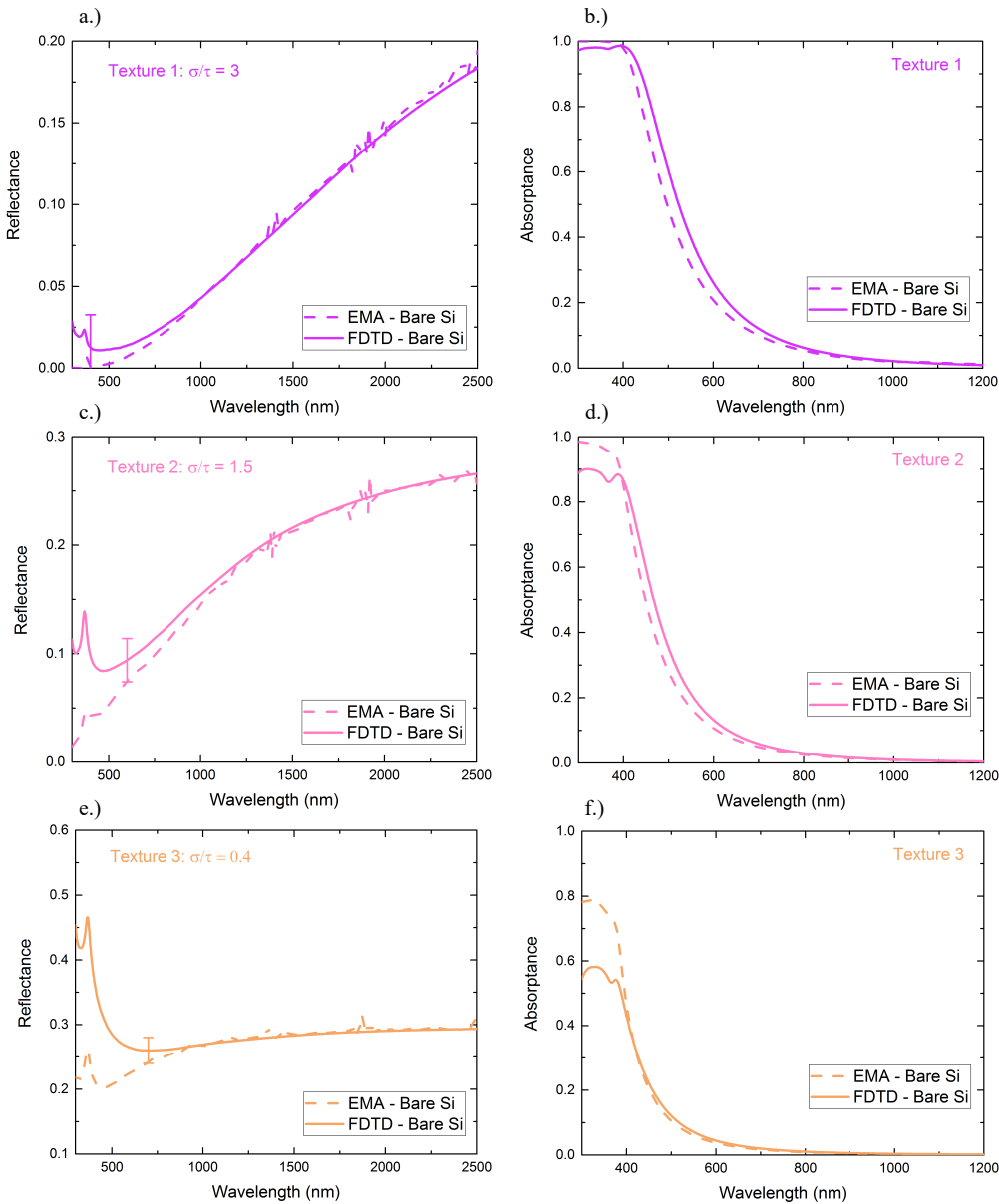


Fig. 5. Simulated reflectance (a, c and e) and absorption (b, d and f) spectra for bare textured silicon, obtained by FDTD (solid lines) and EMA (dashed). The vertical bar shows $\pm 2\%$ absolute difference.

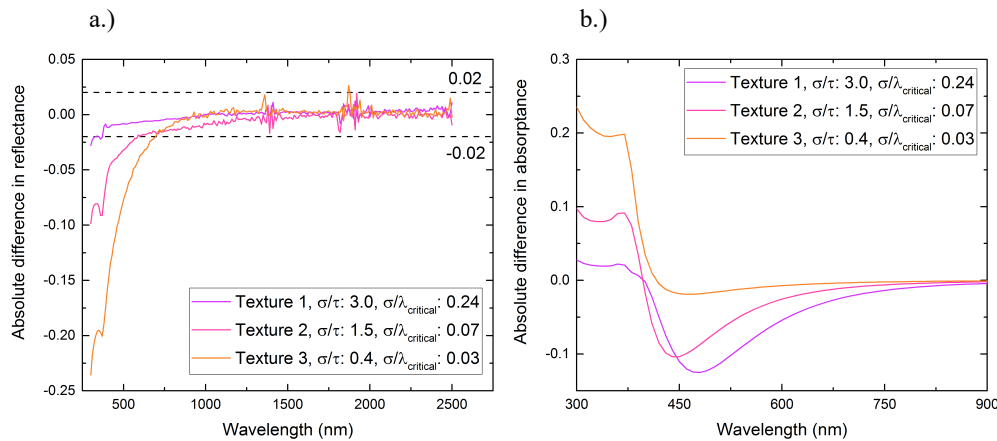


Fig. 6. (a) Absolute difference in simulated reflectance between EMA and FDTD for Texture 1 to 3. The dashed lines indicate the 2% absolute difference. $\lambda_{\text{critical}}$ represents the wavelength at which the absolute difference reaches 2%. (b) Absolute difference in simulated absorptance within the nanotexture between EMA and FDTD.

For all textures, the EMA model consistently overestimates the absorption for wavelengths less than 400 nm (Fig. 6(b)), which is related to the corresponding significant underestimation in the reflectivity at those wavelengths. For Texture 1, EMA underestimates the absorption within the nano-texture by up to 10% between 400 and 800 nm, while the simulated reflectance is also slightly underestimated in that wavelength range. The underestimation in absorption could be due to light scattering that is neglected in EMA, which would result in an underestimation of the optical path length within the nanotexture.

3.2. Electric field intensity distributions of light incident on the nanotexture

The electric field intensity distributions on all textures at 400 nm and 1000 nm (Fig. 7) provide insight into the deviation between EMA and FDTD. At 400 nm, a complex electric field intensity distribution is observed for all textures. We attribute this to strong resonance and multiple light scattering events from the textures, since the incident wavelength is similar to the feature size. The pattern observed in Fig. 7 is the result of interference between the plane wave and the scattered light. These prominent scattering effects are all accurately accounted for in the FDTD simulation. On the other hand, when the wavelength of the incident plane-wave increases to 1000 nm, there is no significant lateral disturbance in the electric field distribution. This indicates that scattering of light from these textures is negligible at 1000 nm and the reflection from these textures is mostly specular. The above results suggest that the discrepancy between EMA and FDTD present in Fig. 6 is due to the fact that near-field effects are not accounted for in the EMA model, which becomes prominent as the wavelength reduces. It is worth noting that a rather complex electric field intensity distribution was observed for texture 1 at 400 nm, yet the total reflectance resulted from FDTD was low such that it was still within 2% absolute difference compared to EMA.

3.3. Effective medium approximation for silicon coated with a dielectric

Figure 8 shows the reflection and absorption spectra of silicon conformally coated with a 100 nm thick dielectric layer from the EMA model compared to the FDTD calculations. The anti-reflection effect is clearly seen in the reduction in reflectance over the entire spectral range, compared to Fig. 5, with an interference minimum at 500 nm, 550 nm, and 800 nm, for Textures

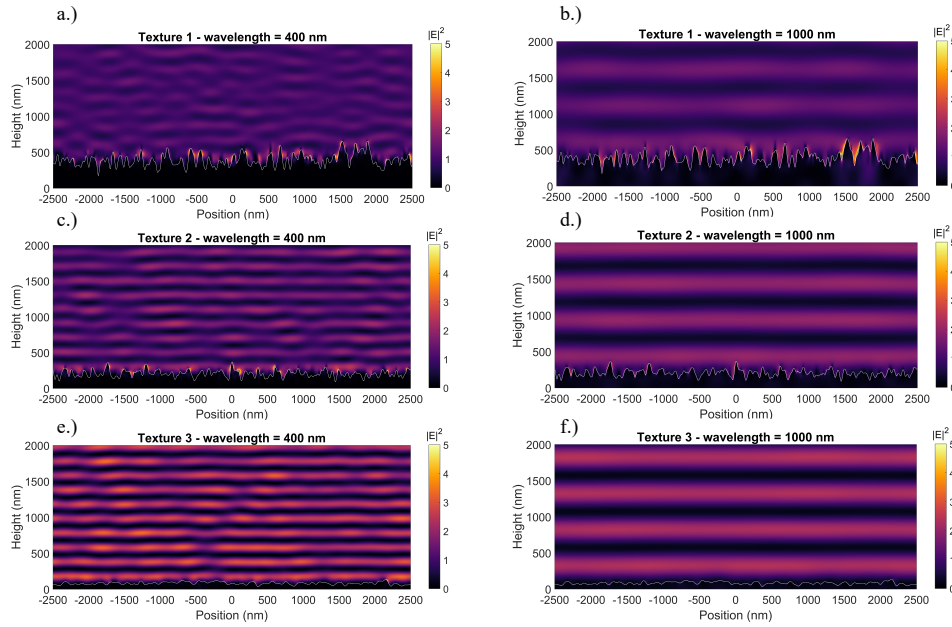


Fig. 7. FDTD calculation of the electric field intensity distribution through a cross-section (highlighted by red curve) of the three bare silicon textures upon plane-wave illumination at a wavelength of 400 nm (a, c and e) and 1000 nm (b, d and f).

1, 2 and 3, respectively. In this case, very good agreement in simulated reflectivity between the EMA model and FDTD calculations is achieved for the whole spectral range examined for Texture 1 and 2 with an absolute difference less than 2%, except in the region ($\lambda \approx 1900$ nm) where signal noise caused by the statistic involved in ray-tracing (Fig. 9(a)). This issue may be resolved by increasing the number of rays used in the Monte Carlo ray tracing simulation. For Texture 3, the absolute difference from 750 nm and higher is less than 2% whilst it increases below 700 nm; the absolute difference reaches 15% at 380 nm. These results indicate the validity of the EMA model for AR-coated textured Si for small σ/λ . This enables EMA as a modelling technique to predict the optical properties of a given nanotexture with a conformal dielectric coating. Similar to the case for the bare texture, very good agreement is observed for the absorption spectra in Fig. 8, with the largest deviation found for short wavelengths for Texture 3 (Fig. 9(b)).

3.4. Proposed criteria for approximating electromagnetic theory by EMA

Figure 10 depicts the same data as shown in Fig. 2, but now both axes are wavelength-normalized and diagonal lines correspond to σ/τ values. This representation reveals the influence of individual change in σ or τ relative to the wavelength. In addition to the specular, geometric-optics, and electromagnetic regions as taken from Tang *et al.*, we define any texture as specular that has a roughness at least 100 times smaller than the wavelength. The EMT regions is proposed in this study and defined where the total simulated reflectance from EMA is within 2% absolute difference to FDTD simulation for silicon textures. The EMT fades to white, indicating a region that is out of scope of this study.

Alternative to the random structures considered in this work to achieve low reflection, ordered structures (silicon cylinders) that support Mie resonances can also be employed to achieve black silicon [41–45]. Using the reported height, pitch and diameter, the σ and τ of these periodic silicon textures were calculated by using “*Gwyddion*” and analytical formulas. We find that these

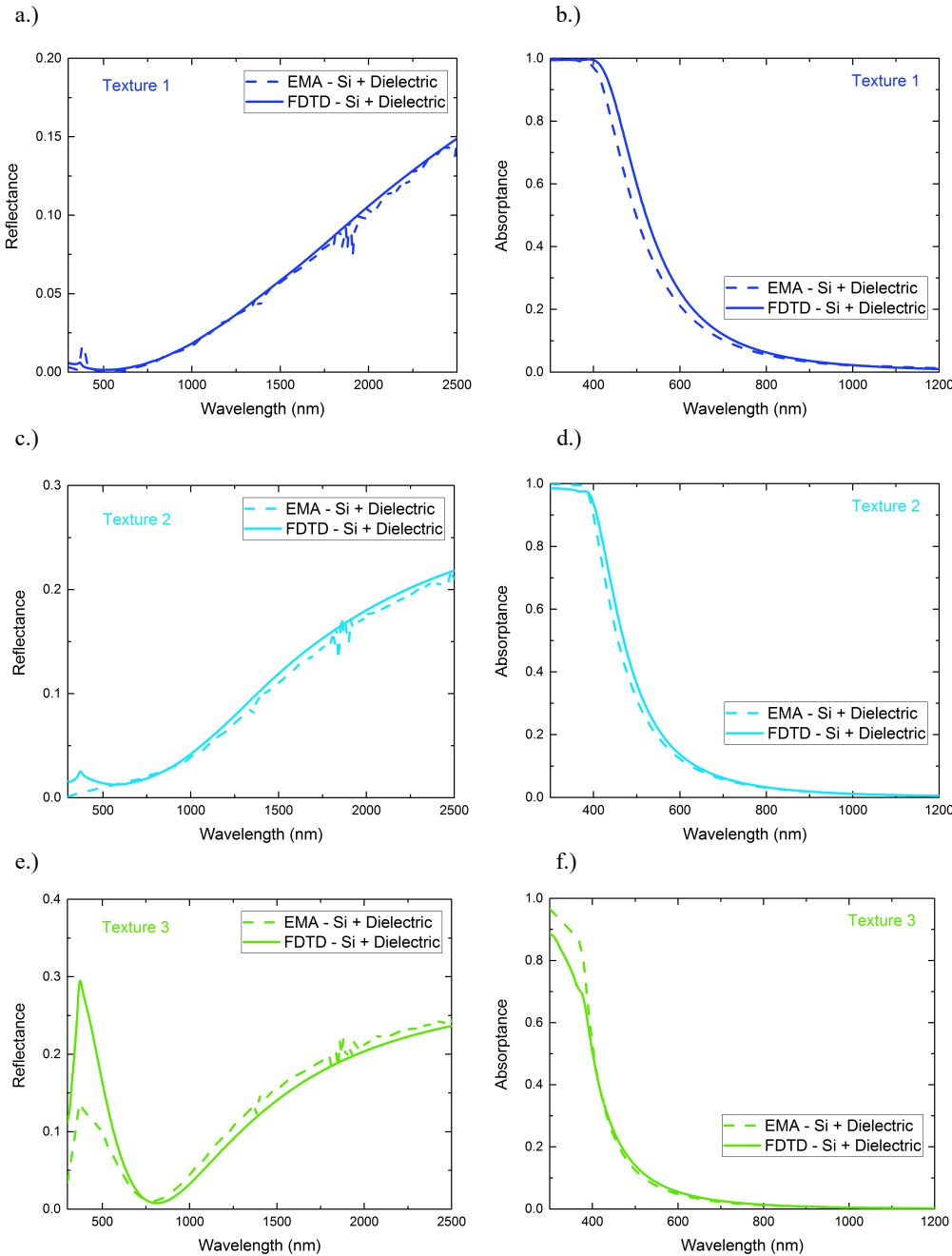


Fig. 8. Simulated reflection (a, c and e) and absorption (b, d and f) within the texture for bare silicon coated with dielectric, obtained by FDTD (solid lines) and EMA (dashed).

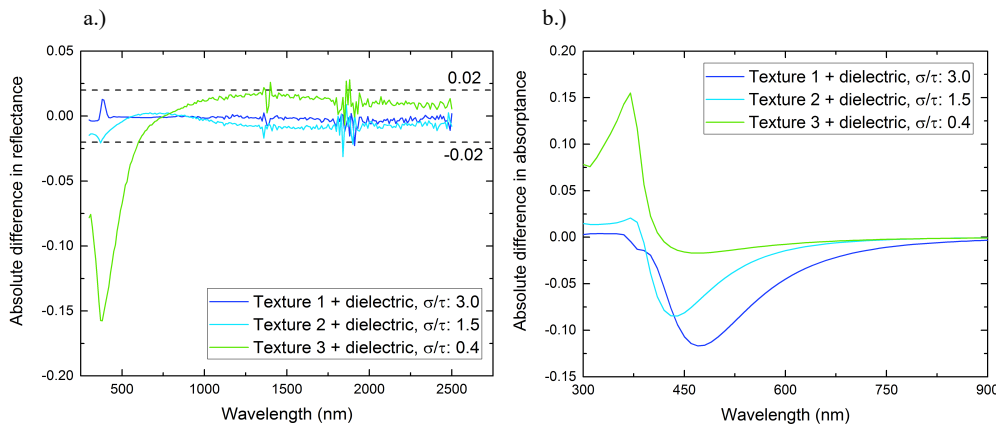


Fig. 9. (a) Absolute difference in simulated reflectance between EMA and FDTD for Texture 1 to 3 coated with dielectric layer. The dashed lines indicate the 2% absolute difference. $\lambda_{\text{critical}}$ represents the wavelength at which the absolute difference reaches 2%. (b) Absolute difference in simulated absorptance within the nanotexture between EMA and FDTD.

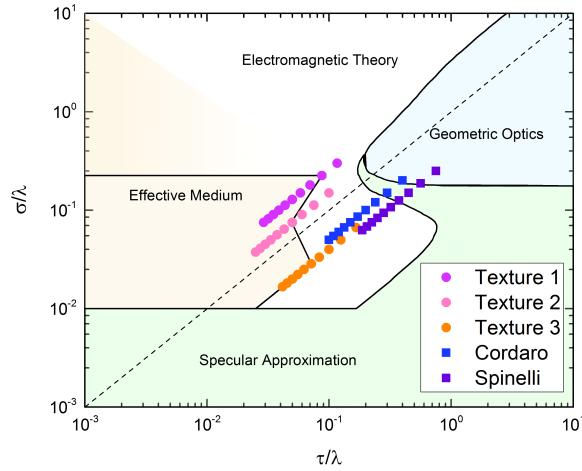


Fig. 10. Diagram of wavelength-normalized roughness versus wavelength-normalized correlation length, with regions of specular reflection (green), geometric optics (green-blue), and the electrodynamic region (blue) as taken from Tang et al. (same data as in Fig. 2). The criteria proposed in this study are indicated in orange, where the total simulated reflectance from EMA is within 2% absolute difference to FDTD simulation for silicon textures. Each dot indicates one of the textures at a 100 nm wavelength interval between 300 and 1200 nm (right to left). The coloured squares are taken from [42,46], respectively. The diagonal dashed line depicts the $\sigma/\tau = 1$ line.

textures do not fall in the electromagnetic region (coloured squares) at 550 nm (the middle of the visible spectrum) or lower. This indicates that the validity regions in this study are typical to random textures, and not valid for ordered/resonant structures.

The validity chart reveals a region within which neither geometric optics nor EMA are adequate for calculating the reflectivity of a textured surface, and where FDTD or other approaches are required. It is interesting to consider how this impacts the modelling of textures typically used in

photovoltaics. Table 1 summarizes the surface characteristic of a variety of common photovoltaic textures based on reports in the literature and AFM measurements made as part of this work. For each texture, the table provides the wavelength for normally incident light at which the boundaries of validity of EMA is crossed. The corresponding SEM images of these textures were shown in Fig. 11.

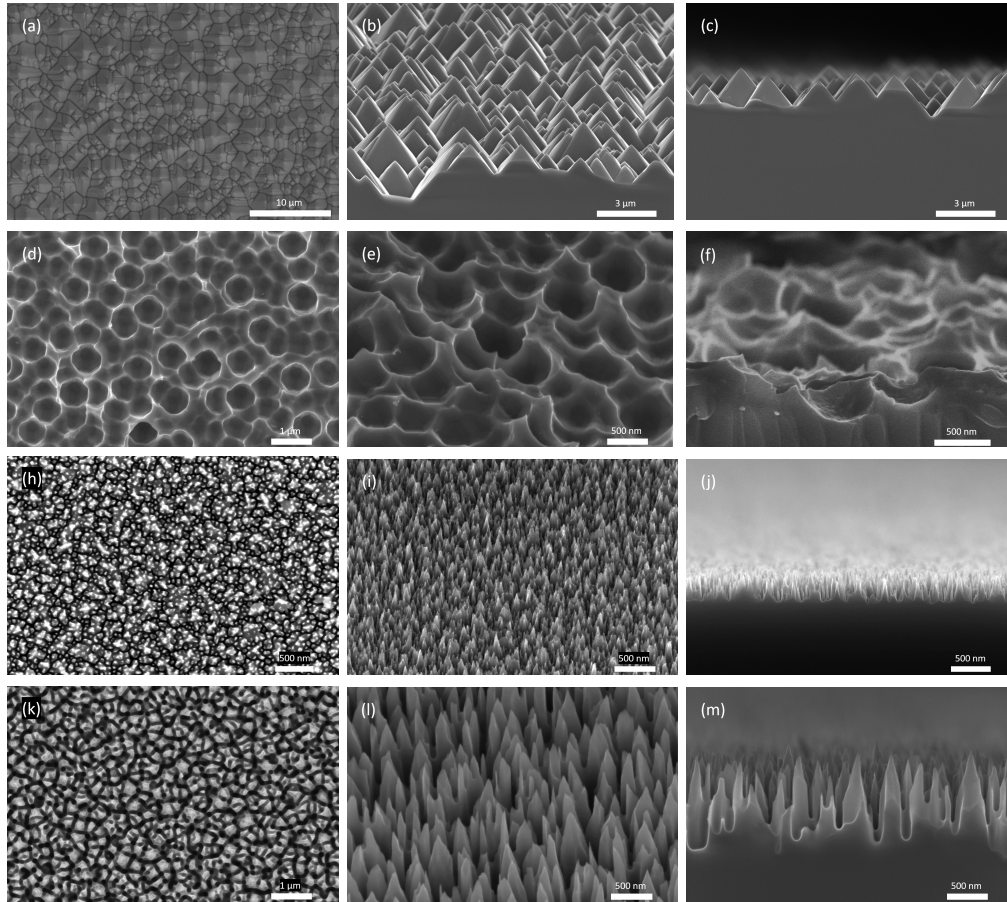


Fig. 11. Top view, 45° and cross-sectional SEM images of random pyramid (a, b and c), metal-assisted chemical etching (d, e and f), shallow reactive-ion etching (h, i and j) and deep reactive-ion etching (k, l and m).

Table 1. Summary of surface characteristics and weighted reflectance between 300 nm – 950 nm for upright random pyramids (RPD), industrial metal-assisted chemical etching (MACE) and reactive-ion etching (RIE) and their regions of validity.

Texture	σ (nm)	τ (nm)	R _{weighted} (%)	GO valid max λ (μm)	Specular max λ (μm)	EMA ^a min λ (μm)
RPD	481	1213	0.119	2.5	4	17
MACE	146	322	0.198	0.9	1.1	5
Shallow RIE	52	55	0.104	N/A	N/A	1
Deep RIE	234	137	0.007	0.7	0.8	3

^aProposed in this work.

For macroscopic random pyramid texture, the geometric optics region applies for wavelengths below 2.5 μm, which implies that 99% of the energy in AM 1.5G spectrum can be accurately simulated by ray-tracing. Beyond 2500 nm, it crosses into the specular region, at which point the simulated results from ray-tracing become less accurate, at least when the angular distribution is of concern. The minimum wavelength for using EMA to model random pyramid is 17 μm, which is beyond the interests in the applications of photovoltaics.

Metal-assisted chemical etched (MACE) texture falls into the geometric optics region up to approximately 900 nm, beyond which it starts to cross into the specular region. This suggests that while the front surface reflectance of MACE maybe accurately simulated by ray-tracing, the internal light trapping (900 nm – 1200 nm, where angular distribution is crucial) may not. As the MACE texture continuously reduces in size, this problem may become more significant in the future. The table also suggests that the parasitic absorption (1000 nm – 4000 nm) of MACE textured silicon solar cells require rigorous solving. Nevertheless, the atmospheric window (8 μm – 13 μm [47]) falls into the proposed effective medium region, which indicates that EMA can be used to rapidly simulate the optical properties of MACE textures when radiative heat loss is concerned [7][47].

RIE-needles may form on a polished surface or a micro-textured surface [48][49]; the former requires deep features to significantly reduce the front surface reflectance, whilst the later often requires shallower features for optimizing the electrical properties of the final device. Therefore, a vast range of surface characteristics are possible. Two options used in this work are shown in Table 1. Nevertheless, it can be observed that neither geometric nor effective medium approximation is fully valid for simulating any of these RIE textures within 300 nm – 1200 nm, the wavelength range that is most relevant to solar cells. Like MACE texture, the atmospheric window of RIE textures falls into the effective medium region.

4. Conclusions

Rapid modelling of nanotextures can enable their integration into large and multi-variant simulations. This is particularly useful for the solar industry to optimise the front surface region and to determine the impact on a cell, module and system level. To enable this, the work presented here investigated the use of the effective medium approximation to model the optical properties of dielectric-coated nanotextures for photovoltaic applications. The validity of this approach was studied not just for a single specific texture, but as a function of feature size. Thus, allowing it to be applied to a broad range of textures. Randomly generated surfaces were used to allow the creation of specific size distributions and to avoid errors related to the topographical characterisation of these surfaces. By comparing the reflection and absorption simulated via EMA and FDTD it identified a region of validity in which the agreement between the techniques for normally incident light was less than 2% absolute. This region was based on the results of three surfaces, further work could refine this further by including more surfaces and extending the analysis to include varied angles of incidence.

Funding

Australian Renewable Energy Agency (2017/RND009); Nederlandse Organisatie voor Wetenschappelijk Onderzoek.

Acknowledgments

This work was supported by the Australian Government through the Australian Renewable Energy Agency (ARENA: 2017/RND009). Responsibility for the views, information, or advice expressed herein is not accepted by the Australian Government. The Dutch part of this work is

part of the research program of the Netherlands Organisation for Scientific research (NWO). We acknowledge the SARA supercomputer facilities and electronic microscopic unit (UNSW).

Disclosures

The authors declare no conflicts of interest.

References

1. ITRPV, *International Technology Roadmap for Photovoltaic (ITRPV)*, (2019), (10th Edition).
2. S. A. Pelaez, C. Deline, S. M. Macalpine, B. Marion, J. S. Stein, and R. K. Kostuk, "Comparison of Bifacial Solar Irradiance Model Predictions with Field Validation," *IEEE J. Photovolt.* **9**(1), 82–88 (2019).
3. G. T. Klise and J. S. Stein, *Models Used to Assess the Performance of Photovoltaic Systems*, (Sandia National Laboratory,2009), (8258).
4. M. Abbott, K. Mcintosh, B. Sudbury, J. Meydbray, T. H. Fung, M. Umair, Y. Zhang, S. Zou, X. Wang, G. Xing, G. Scardera, and D. Payne, "Annual energy yield analysis of solar cell technology," in *46th IEEE PVSC* (2019), pp. 1–5.
5. M. R. Vogt, T. Gewohn, K. Bothe, C. Schinke, and R. Brendel, "Impact of using spectrally resolved ground albedo data for performance simulations of bifacial modules," *Proc. 35th Eur. Photovolt. Sol. Energy Conf. Exhib. (October)*, 1011–1016 (2018).
6. C. K. Lo, Y. S. Lim, and F. A. Rahman, "New integrated simulation tool for the optimum design of bifacial solar panel with reflectors on a specific site," *Renewable Energy* **81**, 293–307 (2015).
7. R. Couderc, M. Amara, and M. Lemiti, "In-depth analysis of heat generation in silicon solar cells," *IEEE J. Photovolt.* **6**(5), 1123–1131 (2016).
8. A. Riverola, A. Mellor, D. Alonso Alvarez, L. Ferre Llin, I. Guerracino, C. N. Markides, D. J. Paul, D. Chemisana, and N. Ekins-Daukes, "Mid-infrared emissivity of crystalline silicon solar cells," *Sol. Energy Mater. Sol. Cells* **174**, 607–615 (2018).
9. M. Steglich, M. Zilk, A. Bingel, C. Patzig, T. Käsebier, F. Schremppel, E. B. Kley, and A. Tünnermann, "A normal-incidence PtSi photoemissive detector with black silicon light-trapping," *J. Appl. Phys.* **114**(18), 183102 (2013).
10. M. Steglich, M. Oehme, T. Käsebier, M. Zilk, K. Kostecki, E. B. Kley, J. Schulze, and A. Tünnermann, "Ge-on-Si photodiode with black silicon boosted responsivity," *Appl. Phys. Lett.* **107**(5), 051103 (2015).
11. J. Lv, T. Zhang, P. Zhang, Y. Zhao, and S. Li, "Review application of nanostructured black silicon," *Nanoscale Res. Lett.* **13**(1), 2523 (2018).
12. M. Steglich, T. Käsebier, M. Zilk, T. Pertsch, E. B. Kley, and A. Tünnermann, "The structural and optical properties of black silicon by inductively coupled plasma reactive ion etching," *J. Appl. Phys.* **116**(17), 173503 (2014).
13. S. Ma, S. Liu, Q. Xu, J. Xu, R. Lu, Y. Liu, and Z. Zhong, "A theoretical study on the optical properties of black silicon," *AIP Adv.* **8**(3), 035010 (2018).
14. M. Kroll, T. Käsebier, M. Otto, R. Salzer, R. B. Wehrspohn, E.-B. Kley, A. Tünnermann, and T. Pertsch, "Optical modeling of needle like silicon surfaces produced by an ICP-RIE process," *Proc. SPIE* **7725**, 772505 (2010).
15. A. J. Bett, J. Eisenlohr, O. Höhn, P. Repo, H. Savin, B. Bläsi, and J. C. Goldschmidt, "Wave optical simulation of the light trapping properties of black silicon surface textures," *Opt. Express* **24**(6), A434 (2016).
16. M. G. Moharam, E. B. Grann, and D. A. Pommet, "Formulation for stable and efficient implementation of the rigorous coupled-wave analysis of binary gratings," *J. Opt. Soc. Am. A* **12**(5), 1068–1076 (1995).
17. N. Tucher, H. T. Gebrewold, and B. Bläsi, "Field stitching approach for the wave optical modeling of black silicon structures," *Opt. Express* **26**(22), A937–945 (2018).
18. N. Tucher, J. Eisenlohr, P. Kiefel, O. Höhn, H. Hauser, M. Peters, C. Müller, J. C. Goldschmidt, and B. Bläsi, "3D optical simulation formalism OPTOS for textured silicon solar cells," *Opt. Express* **23**(24), A1720 (2015).
19. Y. Li, Y. Chen, Z. Ouyang, and A. Lennon, "Angular matrix framework for light trapping analysis of solar cells," *Opt. Express* **23**(24), A1707–A1719 (2015).
20. J. Eisenlohr, N. Tucher, H. Hauser, M. Graf, J. Benick, B. Bläsi, J. C. Goldschmidt, and M. Hermle, "Efficiency increase of crystalline silicon solar cells with nanoimprinted rear side gratings for enhanced light trapping," *Sol. Energy Mater. Sol. Cells* **155**, 288–293 (2016).
21. Ah. A. ELsayed, Y. M. Sabry, F. Marty, T. Bourouina, and D. Khalil, "Optical modeling of black silicon using an effective medium / multi-layer approach," *Opt. Express* **26**(10), 13443–13460 (2018).
22. S. Chattopadhyay, Y. F. Huang, Y. J. Jen, A. Ganguly, K. H. Chen, and L. C. Chen, "Anti-reflecting and photonic nanostructures," *Mater. Sci. Eng., R* **69**(1-3), 1–35 (2010).
23. T. Rahman and S. A. Boden, "Optical modeling of black silicon for solar cells using effective index techniques," *IEEE J. Photovolt.* **7**(6), 1556–1562 (2017).
24. M. Otto, M. Algasinger, H. Branz, B. Gesemann, T. Gimpel, K. Füchsel, T. Käsebier, S. Konermann, S. Koynov, X. Li, V. Naumann, J. Oh, A. N. Sprafke, J. Ziegler, M. Zilk, and R. B. Wehrspohn, "Black silicon photovoltaics," *Adv. Opt. Mater.* **3**(2), 147–164 (2015).
25. K. Tang, R. A. Dimenna, and R. O. Buckius, "Regions of validity of the geometric optics approximation for angular scattering from very rough surface," *Int. J. Heat Mass Transfer* **40**(1), 49–59 (1996).

26. M. M. Plakhotnyuk, M. Gaudig, R. S. Davidsen, J. M. Lindhard, J. Hirsch, D. Lausch, M. S. Schmidt, E. Stamate, and O. Hansen, "Low surface damage dry etched black silicon," *J. Appl. Phys.* **122**(14), 143101 (2017).
27. P. Repo, J. Benick, G. von Gastrow, V. Vähäniemi, F. D. Heinz, J. Schön, M. C. Schubert, and H. Savin, "Passivation of black silicon boron emitters with atomic layer deposited aluminum oxide," *Phys. Status Solidi RRL* **7**(11), 950–954 (2013).
28. B. Bhushan, "Surface roughness analysis and measurement techniques," in *Modern Tribology Handbook* (Taylor and Francis Inc), (2001), p. Chapter 2.2.2.4.
29. D. Bergstrom, "Rough surface generation and analysis," http://www.mysimlabs.com/surface_generation.html (2012).
30. D. Nečas and P. Klapetek, "Gwyddion: An open-source software for SPM data analysis," *Cent. Eur. J. Phys.* **10**(1), 181–188 (2012).
31. D. Payne, M. Abbott, A. C. Lopez, Y. Zeng, T. H. Fung, K. McIntosh, J. Cruz-Campa, R. Davidson, M. Plakhotnyuk, and D. Bagnall, "Rapid optical modelling of plasma textured silicon," in *33rd European Photovoltaic Solar Energy Conference and Exhibition (EUPVSEC)* (2017).
32. E. D. Palik, *Handbook of Optical Constants of Solids I-III*, (Academic Press), (1985).
33. M. Khardani, M. Bouaicha, and B. Bessaïs, "Bruggeman effective medium approach for modelling optical properties of porous silicon: Comparison with experiment," *Phys. Status Solidi* **4**(6), 1986–1990 (2007).
34. B. C. Bergner, T. A. Germer, and T. J. Suleski, "Effective medium approximations for modeling optical reflectance from gratings with rough edges," *J. Opt. Soc. Am. A* **27**(5), 1083 (2010).
35. Y. Battie, A. En Naciri, W. Chamorro, and D. Horwat, "Generalized effective medium theory to extract the optical properties of two-dimensional nonspherical metallic nanoparticle layers," *J. Phys. Chem. C* **118**(9), 4899–4905 (2014).
36. O. Zhuromskyy, "Applicability of effective medium approximations to modelling of mesocrystal optical properties," *Crystals* **7**(1), 1 (2016).
37. J. C. Maxwell Garnett, "Colours in metal glasses and in metallic films," *Philos. Trans. R. Soc., A* **203**(359–371), 385–420 (1904).
38. V. Markel, "Introduction to the Maxwell Garnett approximation: tutorial," *J. Opt. Soc. Am. A* **33**(7), 1244–1256 (2016).
39. M. Losurdo and K. Hingerl, "Ellipsometry at the Nanoscale," in *Ellipsometry at the Nanoscale*, (Springer), (2013), p. 156.
40. Lumerical, "FDTD solution," <https://www.lumerical.com/products/fdtd-solutions/> (2018).
41. Y. Cui, J. Zhu, Z. F. Yu, G. F. Burkhard, C. M. Hsu, S. T. Connor, Y. Q. Xu, Q. Wang, M. McGehee, and S. H. Fan, "Optical absorption enhancement in amorphous silicon nanowire and nanocone arrays," *Nano Lett.* **9**(1), 279–282 (2009).
42. A. Cordaro, J. Van De Groep, S. Raza, E. F. Pecora, F. Priolo, and M. L. Brongersma, "Antireflection high-index metasurfaces combining Mie and Fabry-Pérot resonances," *ACS Photonics* **6**(2), 453–459 (2019).
43. S. Jeong, M. D. McGehee, and Y. Cui, "All-back-contact ultra-thin silicon nanocone solar cells with 13.7% power conversion efficiency," *Nat. Commun.* **4**(1), 1–7 (2013).
44. E. F. Pecora, A. Cordaro, P. G. Kik, and M. L. Brongersma, "Broadband antireflection coatings employing multiresonant dielectric metasurfaces," *ACS Photonics* **5**(11), 4456–4462 (2018).
45. Y. Wang, N. Lu, H. Xu, G. Shi, M. Xu, X. Lin, H. Li, W. Wang, D. Qi, Y. Lu, and L. Chi, "Biomimetic corrugated silicon nanocone arrays for self-cleaning antireflection coatings," *Nano Res.* **3**(7), 520–527 (2010).
46. P. Spinelli, M. A. Verschueren, and A. Polman, "Broadband omnidirectional antireflection coating based on subwavelength surface Mie resonators," *Nat. Commun.* **3**(1), 692 (2012).
47. M. M. Hossain and M. Gu, "Radiative cooling: Principles, progress, and potentials," *Adv. Sci.* **3**(7), 1500360–10 (2016).
48. P. Repo, A. Haarahiltunen, L. Sainiemi, M. Yli-Koski, H. Talvitie, M. C. Schubert, and H. Savin, "Effective passivation of black silicon surfaces by atomic layer deposition," *IEEE J. Photovolt.* **3**(1), 90–94 (2013).
49. A. Ingenito, O. Isabella, and M. Zeman, "Nano-cones on micro-pyramids: modulated surface textures for maximal spectral response and high-efficiency solar cells," *Prog. Photovoltaics Res. Appl.* **23**(11), 1649–1659 (2015).